



Journal of Geophysical Research: Space Physics

RESEARCH ARTICLE

10.1029/2018JA026055

Kev Points:

- Transition time varies in different longitudinal sectors depending on geomagnetic field configuration
- Transition time occurs earlier at higher altitudes
- Solar activity has inconspicuous influence on the longitudinal and altitudinal variation of transition time

Correspondence to:

H. Huang, huanghe@mail.iggcas.ac.cn

Citation:

Huang, H., Lu, X., Liu, L., Wang, W., & Li, Q. (2018). Transition of interhemispheric asymmetry of equatorial ionization anomaly during solstices. *Journal of Geophysical Research: Space Physics*, 123. https://doi.org/10.1029/2018JA026055

Received 2 SEP 2018 Accepted 15 NOV 2018 Accepted article online 26 NOV 2018

Transition of Interhemispheric Asymmetry of Equatorial Ionization Anomaly During Solstices

He Huang^{1,2,3,4} , Xian Lu⁴ , Libo Liu^{1,2,3,5} , Wenbin Wang⁶ , and Qiaoling Li^{1,2,3,5}

¹Key Laboratory of Earth and Planetary Physics, Institute of Geology and Geophysics, Chinese Academy of Sciences, Beijing, China, ²Institutions of Earth Science, Chinese Academy of Sciences, Beijing, China, ³Beijing National Observatory of Space Environment, Institute of Geology and Geophysics, Chinese Academy of Sciences, Beijing, China, ⁴Department of Physics and Astronomy, Clemson University, Clemson, SC, USA, ⁵University of Chinese Academy of Sciences, Beijing, China, ⁶High Altitude Observatory, National Center for Atmospheric Research, Boulder, CO, USA

Abstract The magnitudes of the two crests of equatorial ionization anomaly (EIA) vary with local time. During the solstices, EIA crest in the winter hemisphere is larger than that in the summer hemisphere before noon/early afternoon. Whereafter, the crest in the summer hemisphere becomes intensified, and the stronger EIA crest transits to the summer hemisphere. Using Constellation Observing System for Meteorology, Ionosphere, and Climate ionospheric radio occultation data, we examine the longitudinal and altitudinal variations of this interhemispheric transition in four longitudinal sectors and at seven heights under low/high solar activity conditions. The results show that during the June solstice the transition of the stronger EIA peak from the winter to the summer hemisphere is earlier in the sectors where the geomagnetic equator is further away from the subsolar point and the geomagnetic field declination is larger, while during the December solstice the longitudinal variations generally show the opposite compared with that in the June solstice. The distance between the geomagnetic equator and subsolar point and the geomagnetic field configuration control the upward/downward plasma movements in the summer/winter hemisphere, leading to the different transition times in different longitudinal sectors. For both solstices, transition times emerge earlier as height increases, which is mainly caused by the larger effective scale height in the summer hemisphere than in the winter hemisphere, resulting in a smaller electron density difference at higher altitudes with a fast transition. Solar activity alters the transition time below 320 km, whereas it has no evident effect at higher altitudes.

1. Introduction

Equatorial ionization anomaly (EIA) is a phenomenon in the equatorial ionospheric F layer with two electron density crests at about $\pm 15^{\circ}$ magnetic latitudes and a density trough at the geomagnetic equator (Appleton, 1946; Croom et al., 1959; Duncan, 1960). It is generally believed to be caused by the fountain effect, which lifts the equatorial plasma by upward $\mathbf{E} \times \mathbf{B}$ drifts and redistributes the plasma downward along magnetic field lines under the influence of gravity and pressure gradient forces (Balan et al., 1997; Hanson & Moffett, 1966; Stening, 1992; Zhang et al., 2016). This process is anticipated to form symmetric density humps on both sides of the geomagnetic equator. However, observations of ionospheric critical frequency (foF2), total electron content, and F_2 layer peak electron density (NmF2) have shown interhemispheric asymmetries in both the latitude location and the magnitude of the peaks of the EIA (e.g., Rajaram, 1977; Walker et al., 1994; Yue et al., 2015).

Many researchers have studied this asymmetry by using data from ionosonde chains (Croom et al., 1959; Lyon & Thomas, 1963; Thomas, 1968). They found that foF2 peak was usually larger on the winter side than on the summer side during the daytime and smaller at night. This asymmetry occurs in equinox seasons as well as in solstice seasons (Rao & Malthotra, 1964). In addition, the numerical work by Abur-Robb and Windle (1969) also showed similar characteristics, and they proposed that plasma transport by neutral winds from the summer hemisphere to the winter hemisphere is the dominant factor that leads to the daytime asymmetries, whereas molecular recombination dominates at night and the peak height is much lower in the winter hemisphere than in the summer hemisphere, leading to the nighttime asymmetries. Recently, with the global spatial and temporal coverage of the Constellation Observing System for Meteorology, lonosphere, and Climate (COSMIC) data, a global three-dimensional EIA structure around the June solstice in solar minimum was given by Lin, Liu, et al. (2007). The results indicated that the EIA crest in the winter

©2018. American Geophysical Union. All Rights Reserved.



hemisphere forms earlier in local time than the crest in the summer hemisphere. At the same time, winter crest is stronger than the summer one in the morning. Then the summer crest becomes stronger after 15:00 LT. Further, Tulasi Ram et al. (2009) studied the local time evolution of EIA around both the June and December solstices, obtaining a similar diurnal variation of EIA with that in Lin, Liu, et al. (2007). The time that the larger crest transits from the winter hemisphere to the summer hemisphere (transition time) occurs around 12:00–13:00 LT during the December solstice and is about 2-hr late during the June solstice. They attributed the delay in the transition time in June to the delay in the decrease of the integrated equatorward meridional neutral winds of the respective summer hemisphere in the June than in the December solstice. As the COSMIC data accumulate, Luan et al. (2015) compared the interhemispheric asymmetry of EIA at low and medium solar activity levels and concluded that the transition time was anticorrelated with solar activity.

The mechanism for the interhemispheric asymmetry was proposed to be mainly the relative contribution of the photochemical process and the transport process under different conditions. Walker et al. (1994) suggested that the distance between the crest and the subsolar point might have an effect on the asymmetry, since this might increase the local ion production. On the other hand, the seasonal variation of the relative location of the subsolar point and the magnetic equator might alter the plasma ambipolar diffusion rates. The geomagnetic field configuration also plays an important role in transferring plasma from one hemisphere to another by pushing the plasma up in one hemisphere and down in the opposite hemisphere (Chen et al., 2016; Lin, Hsiao, et al., 2007). The interhemispheric asymmetry has also been studied by using the physics-based National Center for Atmospheric Research Thermosphere-lonosphere Electrodynamics Global Circulation Model. Dang et al. (2016) compared the role of meridional neutral winds, photochemical effects, and magnetic field configuration played in the EIA interhemispheric asymmetry. They confirmed that the trans-equatorial neutral wind is the major contributor to the north-south asymmetry.

In the recent work on the global EIA structure using COSMIC data (Lin, Hsiao, et al., 2007; Tulasi Ram et al., 2009), it is revealed that the magnitude of the interhemispheric asymmetry varies with longitude. The longitudinal differences of the interhemispheric asymmetry were studied by using modeling and observations together at the deep solar minimum of 2008–2010 (Balan et al., 2013). The results revealed that the displacement between geomagnetic and geographic equators and the magnetic declination angle are important in producing interhemispheric asymmetry in different longitudinal sectors. Although there have been some studies on the longitudinal differences of the north-south asymmetry of EIA, the longitudinal variation of the transition time was less studied. Luan et al. (2015) reported that the longitudinal variation of the transition time relies on the solar zenith angle difference between the two hemispheres, but the reason why a large solar zenith angle difference can lead to a different transition time is still not very clear.

As for the altitudinal variation of the EIA interhemispheric asymmetry, Xiong et al. (2013) depicted that EIA crest is stronger in the winter hemisphere from morning to noon and reversed in the afternoon at the Challenging Minisatellite Payload satellite altitude (~400 km), while at the Gravity Recovery and Climate Experiment satellite altitude (~480 km), EIA crest is always stronger in the summer hemisphere for the whole day. Chen et al. (2016) used the ion/electron density data obtained from ROCSAT-1 (~600 km) and Defense Meteorological Satellite Program (~840 km) satellites to investigate the features of the topside EIA. They found that there is no discernable EIA structure at 840 km, while electron densities at 600 km show a larger peak in the winter/summer hemisphere during the June/December solstices at 13:00 LT for F10.7 = 200 sfu. Significant altitude variation of the interhemispheric asymmetry was revealed from these studies. However, a systematic investigation of altitude dependence of the transition times has not been done so far.

Even though many studies have been dedicated to the interhemispheric asymmetry of the EIA peaks, the transition time of this asymmetry and especially its longitudinal and altitudinal variations are less studied and not characterized. At the same time, the mechanisms for such variations are not well understood. To fill in this gap, we use the COSMIC ionospheric radio occultation (IRO) data to study the longitudinal and altitudinal variations of the transition time at four longitude sectors and seven heights during June and December solstices in this work. The 11 years of COSMIC IRO data covering a whole solar cycle have been collected. This enables us to investigate the EIA asymmetry and its variations at lower and higher solar activity levels, respectively. By analyzing the O/N_2 ratio from the Thermosphere lonosphere Mesosphere Energetics and Dynamics/ Global Ultraviolet Imager observations, neutral winds from the Thermosphere Ionosphere Mesosphere Electrodynamics General Circulation Model (TIME-GCM), and the distance between the latitude of subsolar

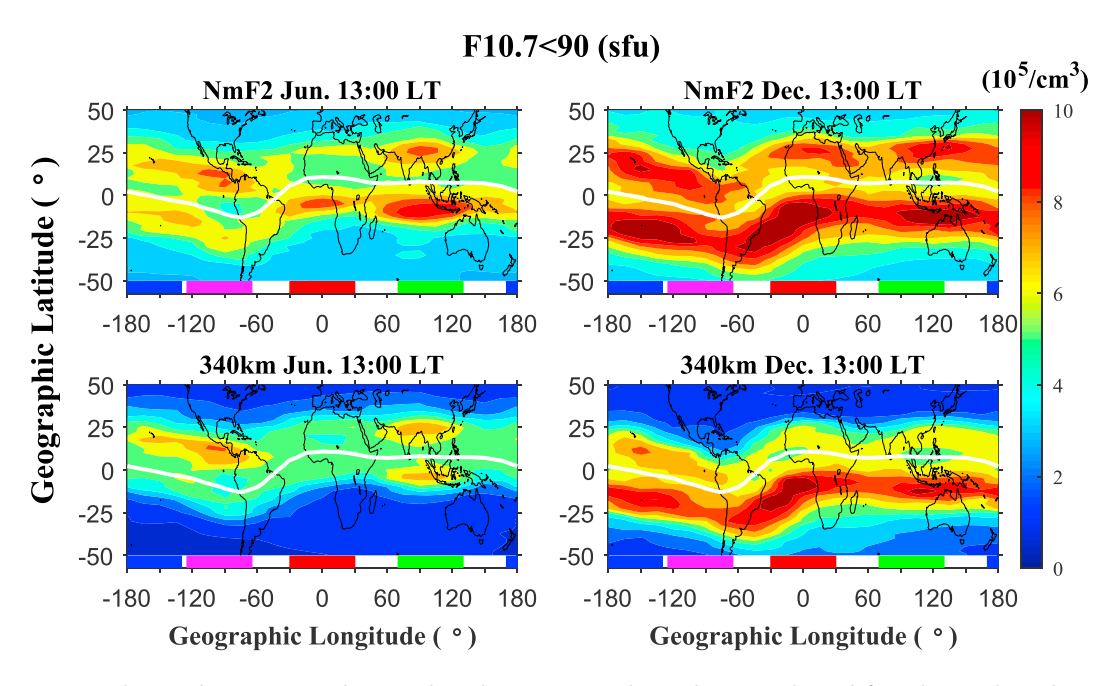


Figure 1. Electron density maps at hmF2 and 340 km at 13:00 LT during the June solstice (left) and December solstice (right) for F10.7 < 90 sfu. The white line stands for the geomagnetic dip equator. Blue, magenta, red and green rectangles indicate four longitudinal sectors of 170° to -130° , -125° to -65° , -30° to 30° , and 70° to 130° , respectively.

point and the location of EIA peaks, we also investigate the possible mechanisms responsible for the longitudinal and altitudinal variations of the transition time.

2. Data and Methodology

COSMIC constellation consists six satellites launched first to an altitude of 500 km, then each satellite entered into their own orbital plane at around 800 km. More than 2,000 radio occultation events per day were recorded in the first 5 years, then the number reduced to 1,000–1,500 for recent years. Each occultation event

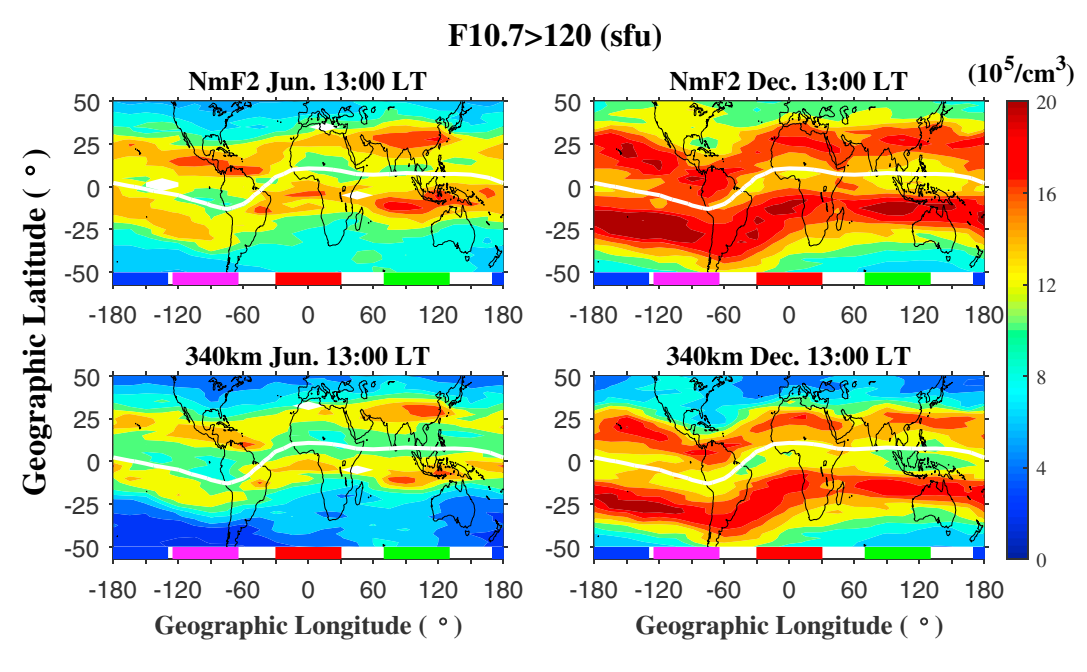


Figure 2. Same as Figure 1, but for F10.7 > 120 sfu.



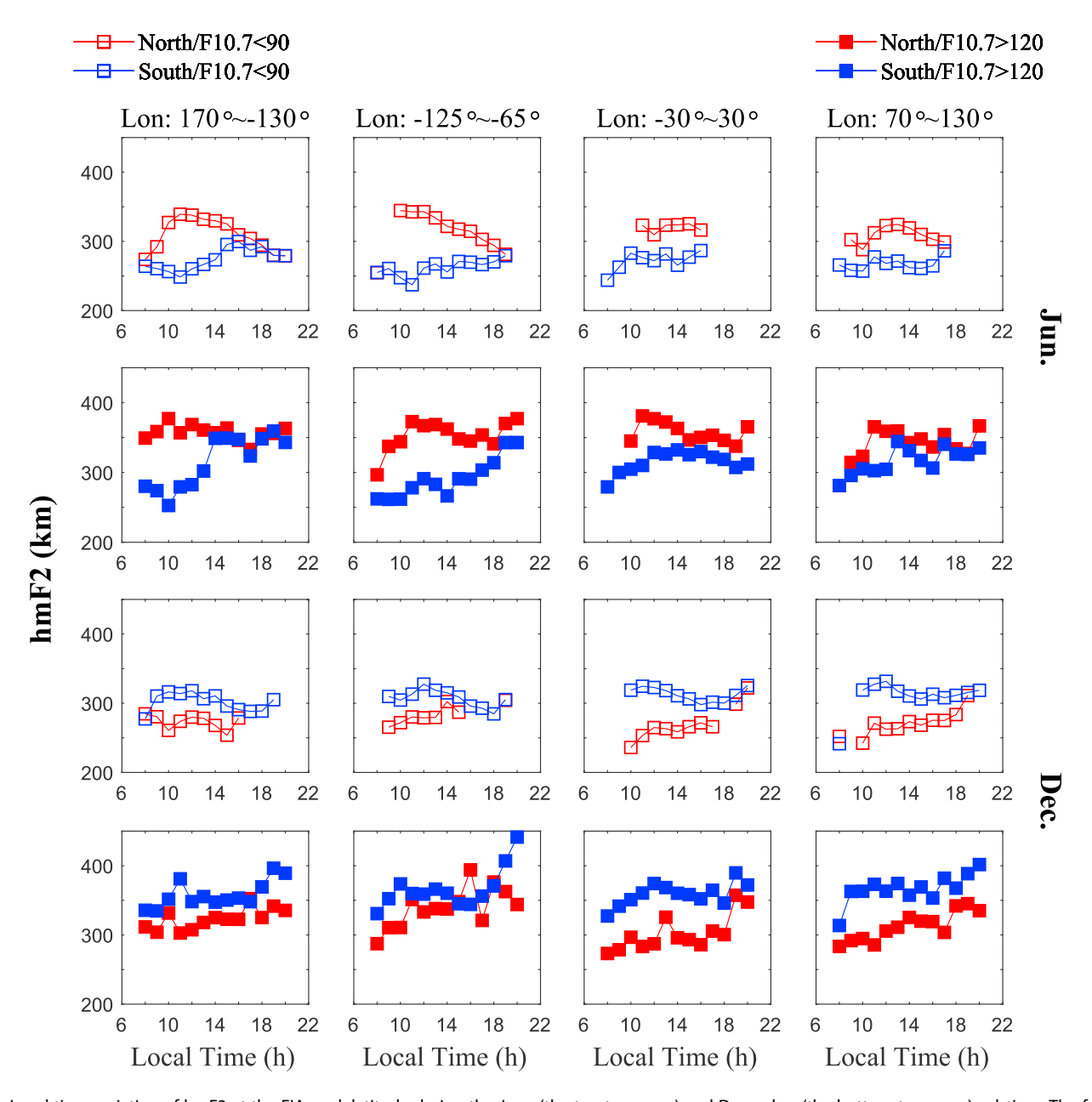


Figure 3. Local time variation of hmF2 at the EIA peak latitude during the June (the top two rows) and December (the bottom two rows) solstices. The four longitudinal sectors are marked on the top on each column. The hollow and the filled squares represent hmF2 under low and high solar activity conditions, respectively. The blue and red lines indicate hmF2 at southern and northern EIA peaks.

can be inverted into an electron density profile (EDP) using the Abel inversion. Although the assumption used by the Abel inversion leads to some discrepancies between electron densities derived from the COSMIC IRO data and other observations in the lower ionosphere, their morphologies are consistent (Chu et al., 2010; Hu et al., 2014; Lei et al., 2007; Yue et al., 2010). COSMIC data have been used in various researches, including the characteristics of the F_2 layer peak electron density (NmF2), F_2 layer peak height (hmF2), slab thickness, and equatorial dynamics, and obtained reasonable results (Guo et al., 2011; He et al., 2009, 2011; Huang et al., 2016; Lin, Wang, et al., 2007; Lin, Liu, et al., 2007; Liu et al., 2009). In this study, we used COSMIC EDPs from day 194 of 2006 to day 180 of 2017, downloaded from the COSMIC Data Analysis and Archive Center. The EDPs have the vertical resolution of approximately 1 km. Being an ionospheric F layer phenomenon, EIA typically appears around hmF2 (\sim 250–400 km at low latitude, depending on different solar activity conditions, seasons, local times, longitudes, and latitudes) and several hundred kilometers above. Meanwhile, most

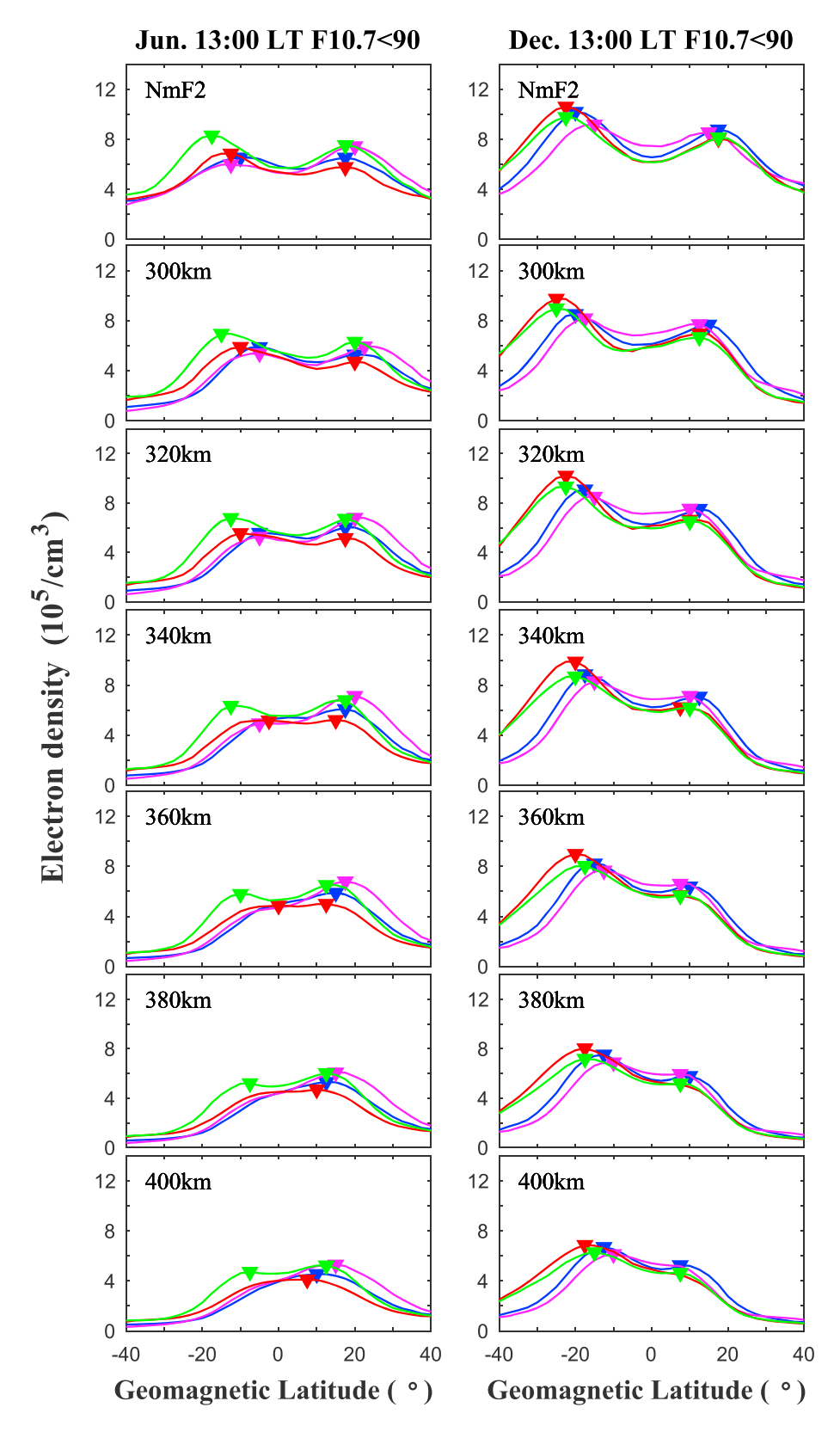


Figure 4. Location and magnitude of equatorial ionization anomaly peaks at 13:00 LT during June (left) and December (right) solstices for F10.7 < 90 sfu. Four color lines indicate the smoothed latitudinal profiles of electron densities in the four longitudinal sectors illustrated in Figures 1 and 2. The triangles mark the locations and the magnitudes of the peaks at different heights. The altitudes are marked in the upper left corner of each panel.

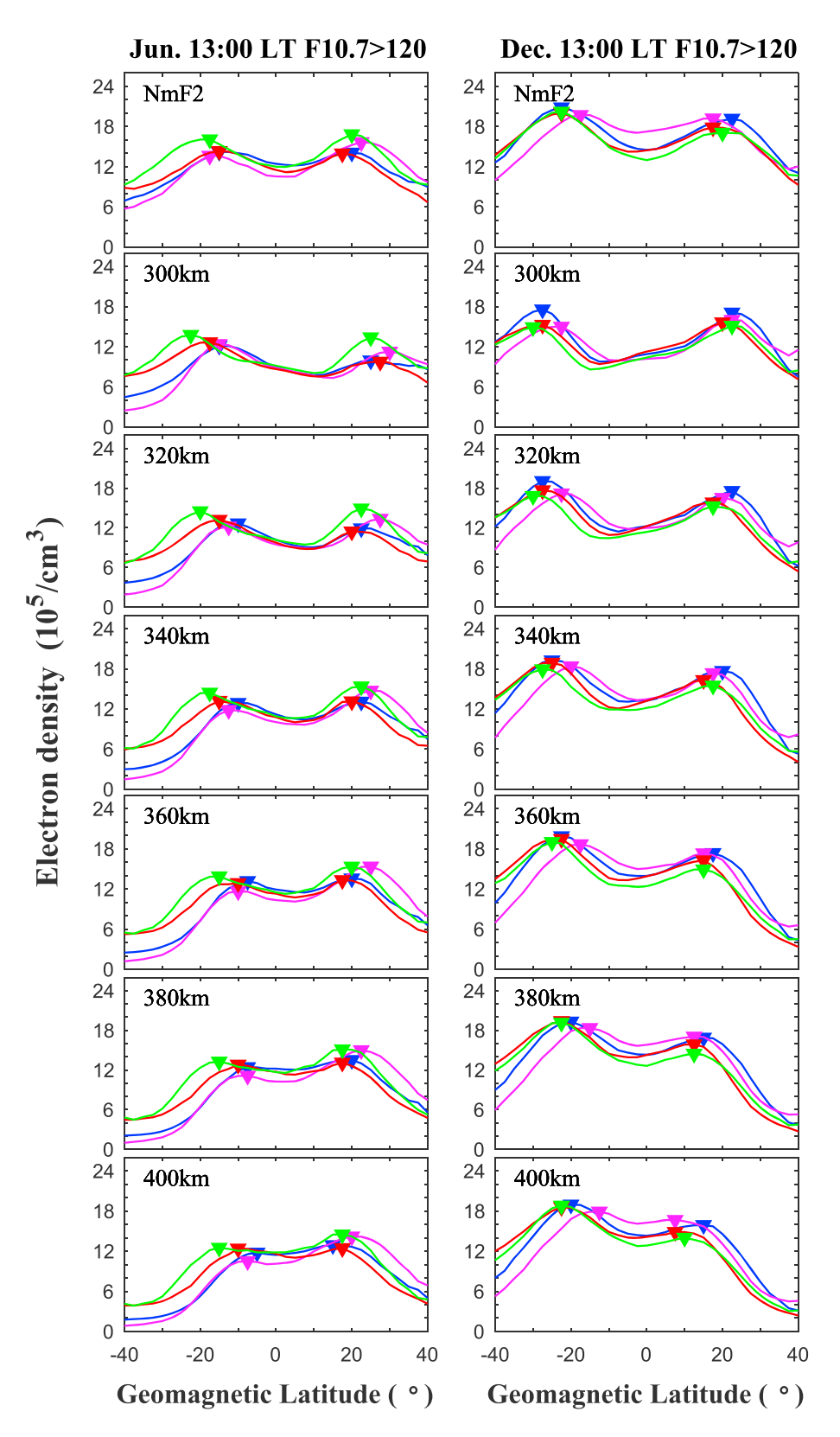


Figure 5. Same as Figure 4, but for F10.7 > 120 sfu.

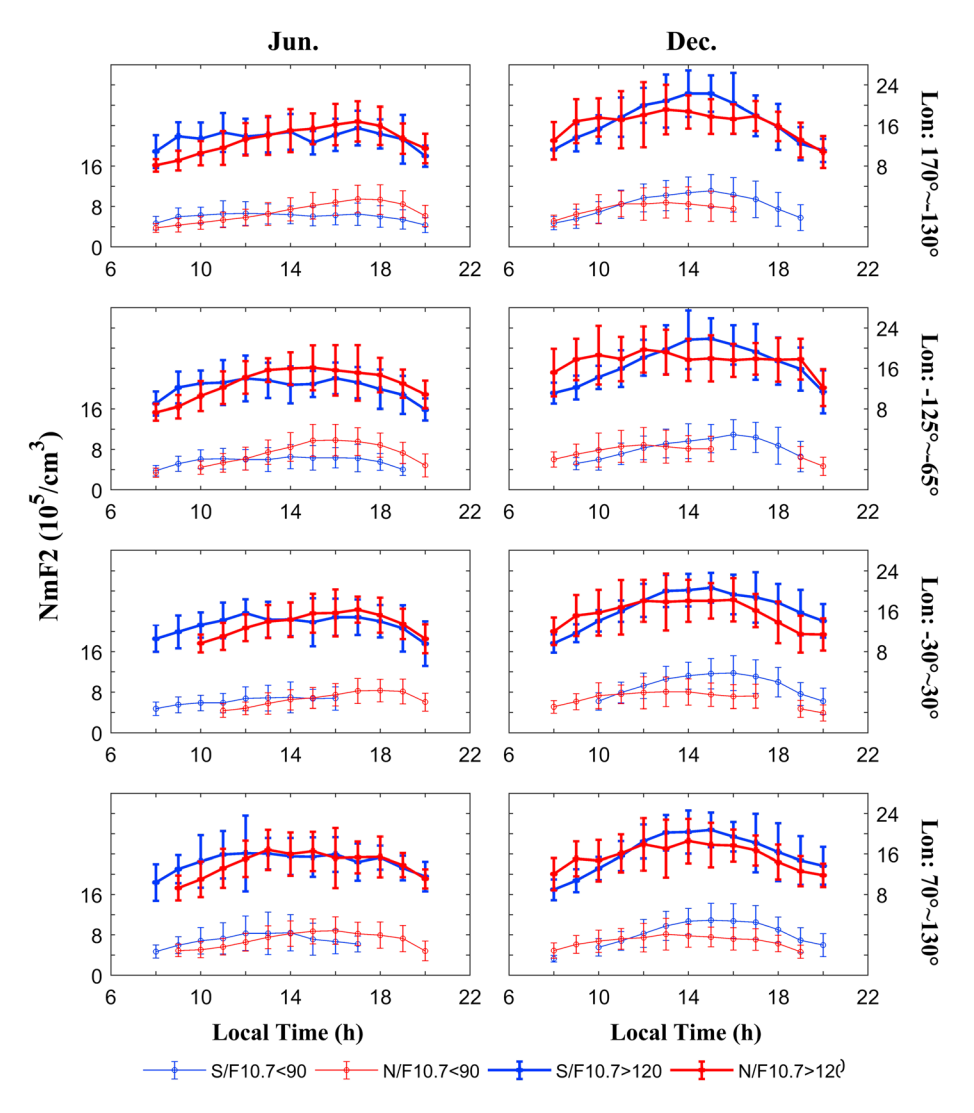


Figure 6. Local time evolution of equatorial ionization anomaly peaks of NmF2 during the June solstice (left) and December solstice (right). Four longitudinal regions are marked to the right of each row. Red and blue lines depict the northern and southern crests with the corresponding standard deviations given as error bars. The thick (thin) solid line with filled (hollow) circles of which the magnitude is given in the right (left) vertical coordinate represents the condition under high (low) solar activity.

COSMIC EDPs were obtained during year 2006–2010. After examining the COSMIC data, we find that there is no obvious EIA phenomenon above 400 km during this deep solar minimum. Thus, we study the electron densities every 20 km from 300 to 400 km along with NmF2 to explore the altitude variation of the transition time. NmF2 are extracted by the following steps. As the altitude gradient of EDPs is very large near the F2 layer peak, the data outliers may introduce uncertainties in the estimation of NmF2 and hmF2, especially when the EDP is very sharp. To avoid this, for each EDP, points above 140 km were smoothed by using 11 points moving average after electron densities smaller than 100 (cm $^{-3}$) or larger than 2 × 10 7 (cm $^{-3}$) being removed. Profiles with a mean deviation (PrfMD) described in equation (1) larger than 0.15 were also rejected. $SEDP_j$ and EDP_j represent the smoothed electron density points and the original electron density points in each profile, respectively. N is the number of data points of the profile.

$$PrfMD = \frac{\sum_{j=1}^{N} \left| SEDP_j - EDP_j \right| / SEDP_j}{N}$$
 (1)

Second, we identified the maximum electron density (npeak) between 170 and 650 km and the corresponding height (hpeak). Then we fitted the EDP within hpeak ± 25 km with a quadratic polynomial. The value and

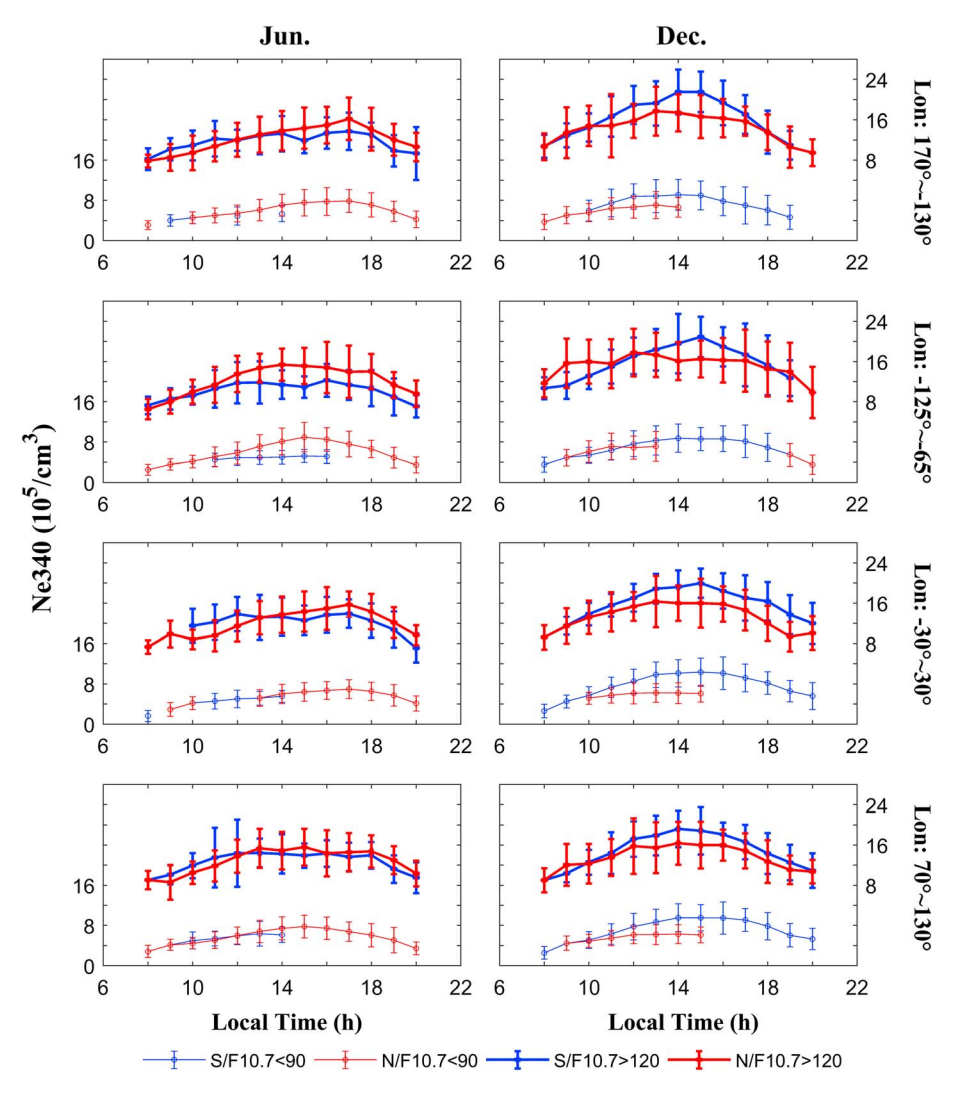


Figure 7. Same as Figure 6, but for electron densities at 340 km.

the location of the vertex are defined as NmF2 and hmF2 of the profile. Profiles with hmF2 lower than 170 km or higher than 650 km were discarded. About 4.29 million pairs of NmF2 and hmF2 were determined by this method.

To obtain the electron density at every 20 km from 300 to 400 km (hereinafter referred to as Neheight), a 7-point running mean is sufficient to remove data outliers and retain a reasonable EDP. Then Neheight was linearly interpolated at the given height, and the corresponding latitude and longitude were also interpolated by the nearest neighbor interpolation. The data volume at each altitude level is about 4.4 million points.

Moreover, NmF2/Neheight were grouped into two solstice seasons (±45 days centered on the June and December solstices) with hourly data centered at 08:00, 09:00, ..., and 20:00 LT with a window of 0.9 hr. According to the 10.7-cm solar radio flux index F10.7, NmF2 and Neheight were also grouped into two categories: F10.7 < 90 solar flux units (sfu, 1 sfu = 10^{-22} W·m $^{-2}$ ·Hz $^{-1}$) and F10.7 > 120 sfu to represent low and high solar activity levels. The data with Ap > 23 nT were excluded for quiet geomagnetic activity conditions with the same criterion of Zeng et al. (2008). For each group, electron density observations were averaged to construct a longitude versus latitude map covering -180° to 180° in longitude and -50° to 50° in latitude with a longitudinal and latitudinal resolution of 15° and 2.5°, respectively. Considering that EIA structures fade rapidly with height during the period we studied, at altitudes higher than 340 km there may be lack of obvious EIA structures at some longitudinal sectors and in a particular season. Therefore, 340 km is the

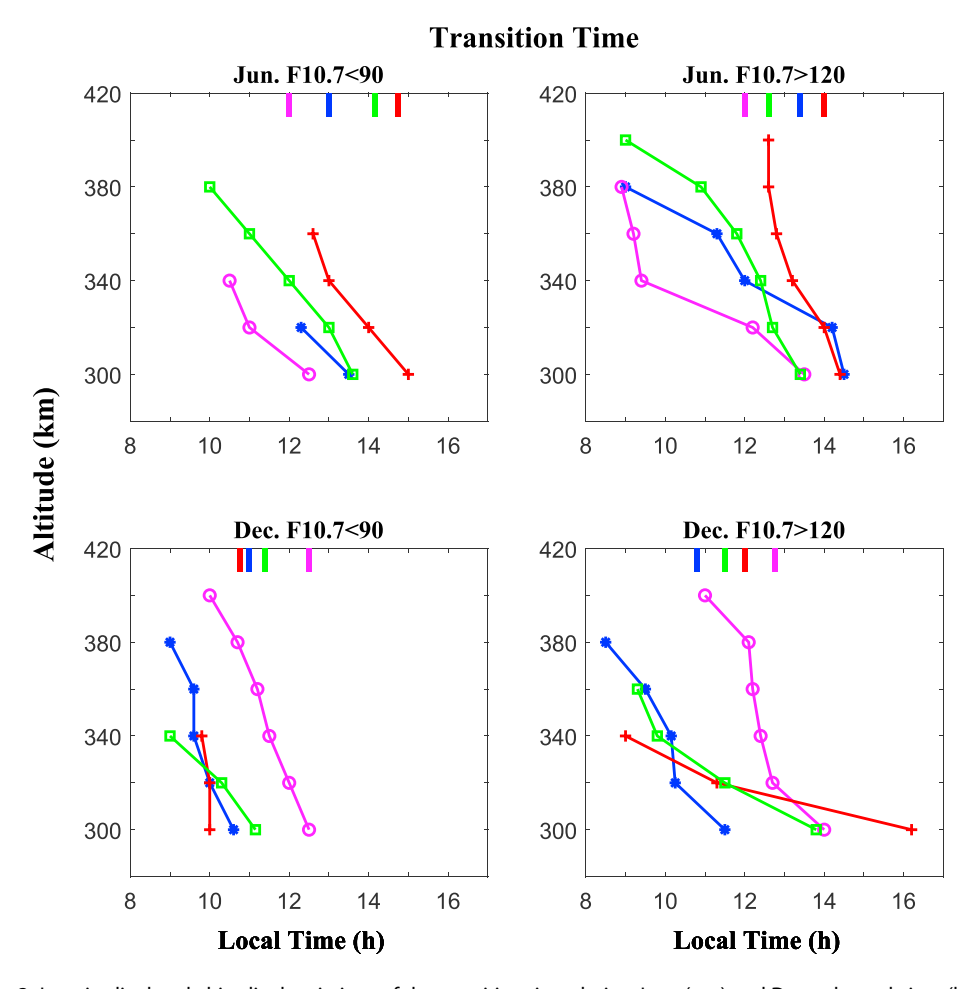


Figure 8. Longitudinal and altitudinal variations of the transition time during June (top) and December solstices (bottom) under low (left) and high (right) solar activity conditions. Four color lines represent the transition time from 300 to 400 km in four longitudinal sectors indicated in Figure 1. The short color bars at the top of the figure mark the transition time of NmF2 in the corresponding longitudinal sectors.

highest altitude that we can show the electron density maps that have clear EIA patterns for all longitudinal sectors and for both seasons. This allows us to give examples of the electron density maps at hmF2 and 340 km at 13:00 LT during the June solstice (Jun. for short) and December solstice (Dec.) under low and high solar activity, shown in Figures 1 and 2, respectively. The white line stands for the geomagnetic equator. A striking feature revealed in both figures is the longitudinal structures of EIA. After we carefully examined all NmF2 and Neheight maps under two solar activity levels, during two seasons and in 13 local time bins, four longitudinal sectors with obvious EIA structures were determined (170° to -130°, -125° to -65° , -30° to 30° , and 70° to 130°) to investigate the longitudinal variations of the transition time. The corresponding longitudinal sectors are indicated by blue, magenta, red, and green rectangles in the bottom of the figures. It is worth noting that the longitudinal structures are not exactly the same during the December and June solstices. In order to keep the consistency between the two seasons, in this work we study the longitudinal variations of the interhemispheric asymmetry with the same longitudinal sectors described above. Figure 3 illustrates the local time variation of hmF2 at the latitude of EIA peaks during the June (the top two rows) and December (the bottom two rows) solstices in the four longitudinal sectors. The hollow and the filled squares represent hmF2 under low and high solar activity conditions, respectively. Blue and red lines indicate hmF2 at southern and northern EIA peaks. From the figure we could conclude that hmF2 is higher in the summer hemisphere than in the winter hemisphere. HmF2 shows different local time evolutions in the four sectors and seasons. For example, the northern (summer) hmF2s reach the maximum, while the southern (winter) ones are the lowest at 10:00 LT in longitudinal

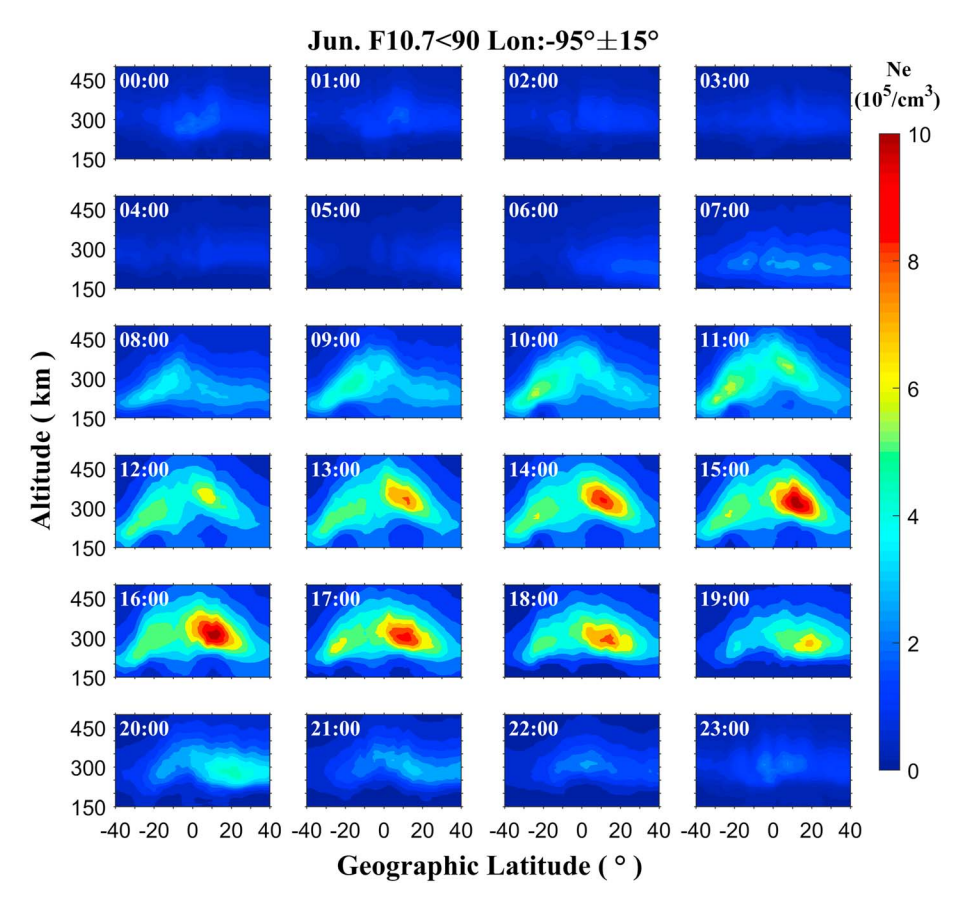


Figure 9. Altitude and latitude variation of the electron density during a day in the June solstice for F10.7 < 90 sfu and in the $-95^{\circ} \pm 15^{\circ}$ longitude sector (the magenta area).

sector 170° to -130° during the June solstice, whereas both the summer and winter hmF2 peak around 11:00-12:00 LT in the sector of -30° to 30° .

In the four longitudinal sectors, we calculated the median of the electron density in each geomagnetic latitude grid from -40° to 40° with a step of 2.5°. The typical number of data points in each altitude (7 altitudinal levels), longitude (4 sectors), latitude (33 bins), local time (13-hr bins), and season (2 solstices) grid are about 120 and 30 for F10.7 < 90 sfu and F10.7 > 120 sfu, respectively. This ensures that statistically meaningful analysis can be made with the data. Next, the latitudinal profile of the electron densities was smoothed with 5point running average for each longitudinal sector. Then EIA crests or a single peak (as height increases, the two crests of EIA merge into one single peak around the geomagnetic equator; Bilitza, 2009; Huang et al., 2015) were determined within ±35° geomagnetic latitude in the Northern and the Southern Hemispheres. Figures 4 and 5 show the location and the magnitude of the EIA peaks marked by triangles from 300 to 400 km as well as NmF2, during the June and December solstices at 13:00 LT for low and high solar activity conditions. The four color lines indicate the smoothed latitudinal profiles of the electron densities at the four longitudinal sectors illustrated in Figures 1 and 2. The altitudes are marked in the upper left corner of each panel. As altitude increases, the distance between the northern and southern peaks and the magnitude of the two peaks decreases. At higher altitudes, there is only one single peak in some longitudinal sectors (red, blue, and magenta sectors at 380/400 km during the June solstice and red and magenta sectors at 400 km during the December solstice) under the condition of F10.7 < 90 sfu. Therefore, in this work, we focus on the transition time below 400 km.

3. Observations and Results

Figures 6 and 7 show the local time evolution of EIA peaks of NmF2 and Ne340 during the June solstice (left) and December solstice (right). Four longitudinal regions are marked to the right of each row. Red and Blue

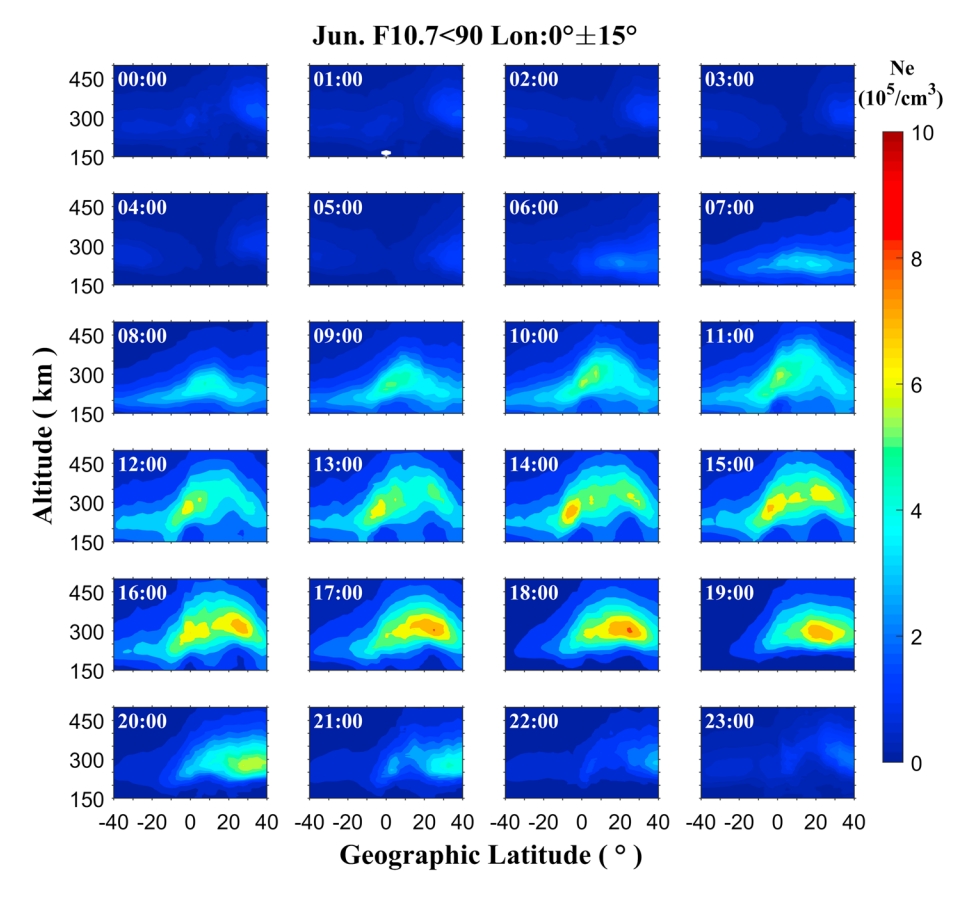


Figure 10. Same as Figure 9, but for $0^{\circ} \pm 15^{\circ}$ (the red area).

lines depict the northern and the southern crests. We calculate standard deviations of all the densities in each longitudinal sector in each altitude and latitude bin. Then the corresponding standard deviations at EIA peak latitudes are marked as error bars in Figures 6 and 7. The thick (thin) solid line with filled (hollow) circles of which the magnitude is given in the right (left) vertical coordinate represents the condition under the high (low) solar activity level. The cross point of the two lines indicates the local time (transition time) when the stronger crest transfers from one hemisphere to another hemisphere. The winter crest is stronger than the summer one in the morning (Dec.) or before the early afternoon (Jun.) at both heights and in the four longitudinal sectors, which is consistent with the previous work (Lin, Liu, et al., 2007; Luan et al., 2015; Tulasi Ram et al., 2009). After the transition time, the stronger crest shifts to the summer hemisphere from the winter hemisphere. The transition times show clear longitudinal variations. For example, the NmF2 transits the earliest at 12:00 LT in longitudinal sector -125° to -65° (magenta sector), while it occurs the latest at 15:00 LT in longitude sector -30° to 30° (red sector) in the June solstice for F10.7 < 90 sfu. This transition time may vary under different solar activity, while the general features do not change. This is also true at other altitudes (320, 360, 380, and 400 km, not shown here).

Figure 8 depicts the longitudinal and altitudinal variations of the transition time during the June (top) and December solstices (bottom) under low (left) and high (right) solar activity. Four color lines represent the transition times from 300 to 400 km in four longitudinal sectors indicated in Figure 1. The short color bars at the top of the figure mark the transition time of NmF2 in the corresponding longitudinal sectors. There are no results above some certain heights, where the two crests have already merged into one single peak. Clear longitudinal differences could be seen from the figure. During the June solstice, Ttm < Ttb < Ttg < Ttr (Ttm, Ttb, Ttg, and Ttr represent the transition times in the four longitudinal regions marked by magenta, blue, green, and red rectangles in Figure 1, respectively) could be observed for the lower solar activity level and for the high solar activity case above 320 km. The early transition time is clear in the sectors where the offset between the dip equator and the geographic equator is larger and the geomagnetic declination is

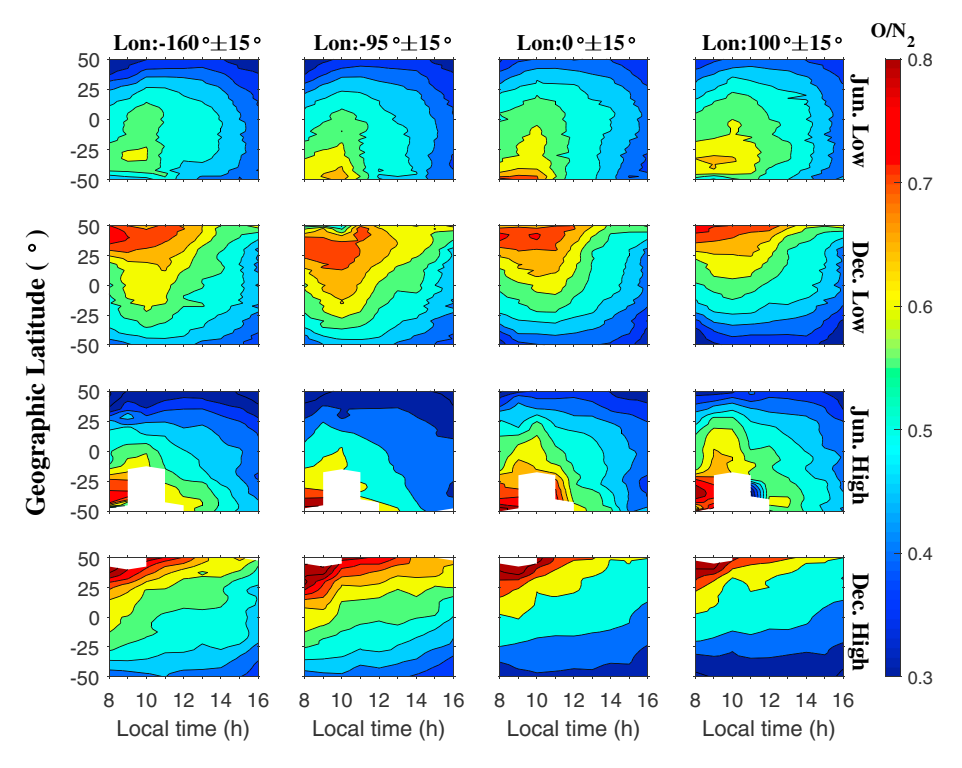


Figure 11. Latitudinal and local time variation of thermospheric O/N₂ ratio obtained from Global Ultraviolet Imager observations under low/high solar activity conditions for both the June and December solstices. Corresponding longitudinal sectors are labeled on the top of each column.

greater (magenta and blue longitudes). Compared with the June solstice, the longitudinal variations of the transition time in the December solstice generally reveal the opposite trend (Tr < Ttg < Ttb < Ttm) above 320 km for F10.7 > 120 sfu. However, under lower solar activity, the transition time does not show a clear longitude dependence in the red, blue, and green longitudes, which appear to move close to each other. Ttm does become the latest compared with the other three transition times (i.e., Ttr, Ttg, and Ttb). It seems that solar activity alters the transition time below 320 km, whereas it has no evident effects at higher altitudes. Such a solar activity effect is more prominent during the June solstice than in the December solstice. As hmF2 is around 250 to 350 km from Figure 3, we could expect that the transition time of NmF2 is similar with that at lower altitude. A uniform feature is that the transition time occurs at earlier local times as height increases for both the solstice seasons and solar activity levels, which has not been reported previously.

To illustrate directly the longitudinal and altitudinal variation of the transition time, we use the longitudinal sectors of $-95^{\circ} \pm 15^{\circ}$ (magenta area) and $0^{\circ} \pm 15^{\circ}$ (red area) as examples. Figures 9 and 10 depict the altitudinal versus latitudinal cross sections of electron densities during a day in the June solstice for F10.7 < 90 sfu. These two longitudinal sectors represent the earliest/latest transition time in the June solstice shown in Figure 8 (magenta and red lines in the upper left panel). The transition times in these two sectors are around 12:00 and 16:00 LT during the June solstice, respectively.

4. Discussion

4.1. The Transition of Interhemispheric Asymmetry of EIA

As mentioned in section 1, both photochemical process and trans-equatorial neutral wind transportation could contribute to the asymmetry of EIA. We examine the latitudinal and daytime variation of thermospheric O/N_2 ratio obtained from the Global Ultraviolet Imager observations in each longitudinal sector under low/high solar activity levels for both June and December solstices. The results are shown in Figure 11. It can be seen that the winter hemisphere to summer hemisphere the O/N_2 ratio latitudinal gradient before noon is much larger than that in the afternoon for all conditions. A larger O/N_2 indicates the production

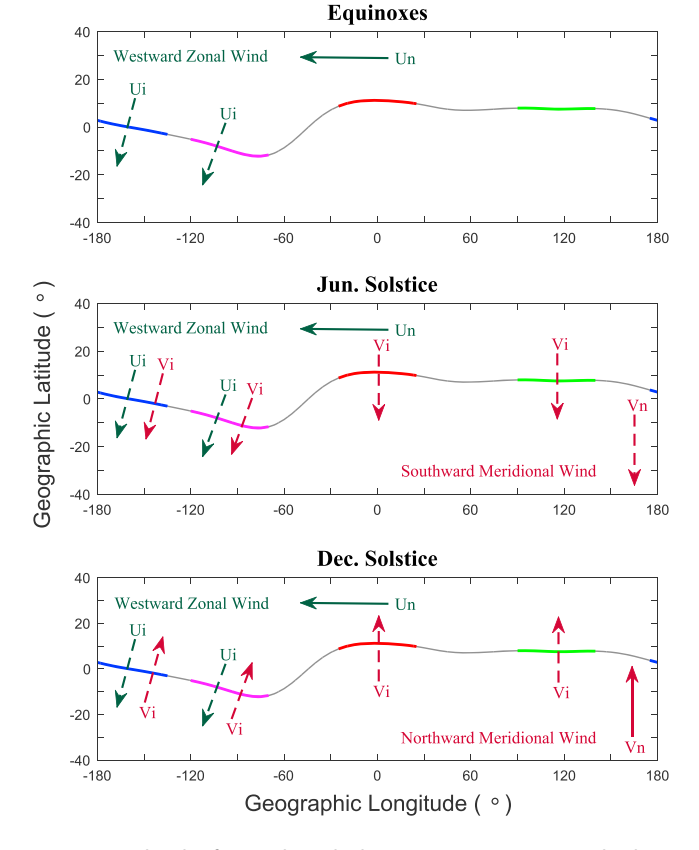


Figure 12. A sketch of neutral winds during equinox seasons and solstices seasons along with the geomagnetic dip equator in the four longitudinal sectors in geographic coordinates. The gray line indicates the dip equator. \mathbf{U}_n and \mathbf{V}_n stand for zonal neutral winds and meridional neutral winds during the corresponding season, respectively. \mathbf{U}_i and \mathbf{V}_i are the field-aligned components of \mathbf{U}_n and \mathbf{V}_n in the geomagnetic field meridional plane, respectively.

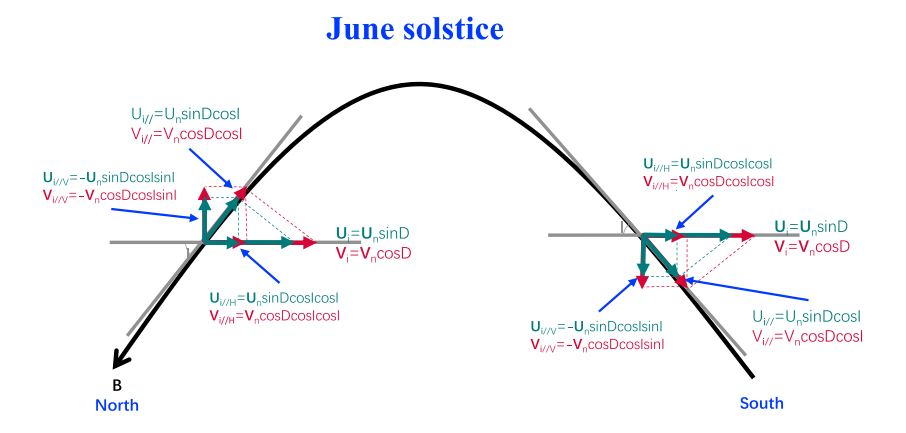
rate of ionization can be greater than the recombination process that can lead to a stronger EIA crest. Thus, the stronger EIA peak appears in the winter hemisphere before local noon. Besides, during the solstice, the neutral wind transports plasma from the summer hemisphere to the winter hemisphere, which has been proposed to be the mechanism to enhance the winter EIA peak in the morning (Lin, Liu, et al., 2007; Luan et al., 2015; Tulasi Ram et al., 2009). After the noontime, O/N_2 ratio becomes smaller in the winter hemisphere while it only decreases slightly in the summer hemisphere. In addition, solar radiation in the summer hemisphere is more intense compared to that in the winter hemisphere. When the difference of O/N_2 between the two hemispheres becomes smaller toward the afternoon, more ionization is produced in the summer hemisphere leading to a stronger EIA peak in the summer hemisphere.

In the meanwhile, the F region ionosphere in the summer hemisphere occurs at a higher altitude than the winter hemisphere one because of the thermal expansion in the summer. Zonal and meridional winds also push up (down) the summer (winter) hemispheric ionosphere, this process is closely related to geomagnetic declination D (eastward as positive) and inclination I (downward as positive). Figure 12 depicts a sketch of neutral winds in three seasons along with the geomagnetic dip equator in the four longitudinal sectors studied in this work in geographic coordinates. The gray line indicates the dip equator. Zonal neutral wind \mathbf{U}_n is generally westward during the daytime in all three seasons (Chen et al., 2016; Ren et al., 2008). Trans-equator neutral wind \mathbf{V}_n is southward during the June solstice and northward during the December solstice. We take \mathbf{V}_n to be zero during equinoxes approximatively, as the Sun insolation on the two hemispheres is roughly symmetric, which results in weak trans-equator winds. $\mathbf{U}_i = \mathbf{U}_n \sin D$ and $\mathbf{V}_i = \mathbf{V}_n \cos D$ are the velocity projection of \mathbf{U}_n and \mathbf{V}_{n} in the geomagnetic field meridional plane. As geomagnetic declination D is small in red and green sectors, the projection of the zonal wind \mathbf{U}_i is close to zero in these two sectors, whereas in the blue and magenta sectors, \mathbf{U}_i cannot be neglected and has the same direction with \mathbf{V}_i in the

June solstice, while the directions are opposite in the December solstice. The corresponding latitudinal and altitudinal cross sections of \mathbf{U}_i and \mathbf{V}_i in the blue or magenta area during the June and December solstices are shown in Figure 13. For the cross sections of the red or green area, the dark green lines (representing **U**_i) can be omitted as mentioned above. The black curved line with arrow and gray straight line stands for the geomagnetic field line and its tangent line, respectively. From Figure 13 we know that \mathbf{U}_i and \mathbf{V}_i push the plasma to move along geomagnetic field lines at a velocity of $\mathbf{U}_{i/l} = \mathbf{U}_n sinDcosl$ and $\mathbf{V}_{i/l} = \mathbf{V}_n cosDcosl$. The horizontal and vertical components of $\mathbf{U}_{i/l}$ are $\mathbf{U}_{i/lH} = \mathbf{U}_n sinDcoslcosl$ and $\mathbf{U}_{i/lV} = -\mathbf{U}_n sinDcosl$ sin l (as plasma vertical $\mathbf{E} \times \mathbf{B}$ drifts is positive upward, which is opposite to the direction of positive I), respectively. Similarly, the corresponding horizontal and vertical components of $\mathbf{V}_{i/\prime}$ are $\mathbf{V}_{i/\prime H} = \mathbf{V}_n cosDcoslcosl$ and $\mathbf{V}_{i/\prime}$ $_{V}=-\mathbf{V}_{n}cosDcoslsinI.$ Thus, the neutral wind causes a vertical plasma motion at the speed of $\mathbf{V}_{Z}= (\mathbf{U}_n sinD + \mathbf{V}_n cosD) cosls inl.$ Under the effects of thermal expansion and neutral winds, the summer hemisphere is uplifted to a higher altitude after about 10:00-11:00 LT (Figure 9) or 12:00-13:00 LT (Figure 10) for the two longitude sectors. The upward movement of the plasma reduces the recombination effect in the summer hemisphere, thus enhancing electron densities. On the contrary, the downward movement of the plasma enhances the recombination effect in the winter hemisphere, which decreases the electron density. This downward/upward vertical movements, therefore, contribute to the stronger EIA crest transferring from the winter hemisphere to the summer hemisphere approximately after local noon.

4.2. Longitudinal Variation of the Transition Time

Clear longitudinal variations in the transition time of the EIA interhemispheric asymmetry can be seen from Figures 8–10. As discussed in sections 1 and 4.1, neutral winds are proposed to be one of the reasons in



December solstice

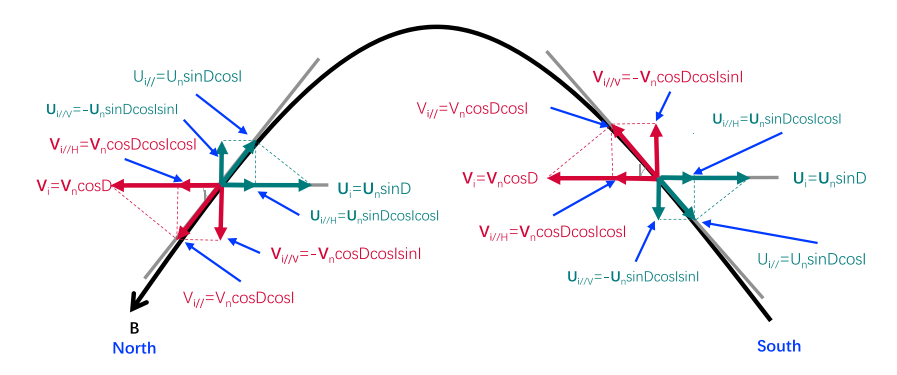


Figure 13. Latitudinal and altitudinal cross sections of \mathbf{U}_i and \mathbf{V}_i in the blue or magenta area during equinox seasons and solstice seasons. The black line with arrow and the gray line stand for the magnetic field line and the tangent line, respectively. $\mathbf{U}_{i//}$ and $\mathbf{V}_{i//}$ are plasma velocities along the geomagnetic line. Their horizontal and vertical components are $\mathbf{U}_{i//H}$ and $\mathbf{V}_{i//H}$, and $\mathbf{V}_{i//H}$, and $\mathbf{V}_{i//H}$, respectively.

producing the interhemispheric asymmetry of EIA. The neutral wind effects rely heavily on the geomagnetic declination and inclination angles as shown in Figures 12 and 13. Hence, the longitudinal variations of D and I could lead to different transition times in different sectors. Hereinafter, we take Figures 9 and 10 (magenta/ red sectors) as examples to discuss the mechanisms for the longitudinal variation of the transition time. During the June solstice, \mathbf{V}_n is southward; \mathbf{U}_n is westward during the daytime as shown in Figure 12 (middle). From the middle panel of Figure 12, \mathbf{U}_i has the same direction as \mathbf{V}_i in the magenta sector, enhancing the upward (downward) plasma transport, which moves the plasma to a higher (lower) altitude where the recombination loss of plasma is smaller (larger) in the summer (winter) hemisphere. However, \mathbf{U}_n has a negligible effect in the red sector as the geomagnetic declination is small there. Thus, the transition occurs early in Figure 9, compared with Figure 10, during the June solstice. On the contrary, \mathbf{U}_i and \mathbf{V}_i are in the opposite direction as indicated in the bottom panel in Figure 12, tending to cancel each other in the magenta area. This will weaken the upward (downward) transport in the summer (winter) hemisphere during the December solstice. Hence, the transition time is later in the magenta sector than in the red sector, which is directly opposite to the case of the June solstice (not shown here). From the discussion above, it is suggested that the geomagnetic declination in different longitudinal sectors and the relative direction between $\mathbf{U}_{i//V}$ and $\mathbf{V}_{i//V}$ modify the transition time during the two solstice seasons.

Moreover, the relative location between the latitude of the subsolar point and the geomagnetic equator (or the location of EIA peaks) also plays a role in the longitudinal variation of the transition time. Figure 14 shows the average geographic latitudes of the two EIA peaks at different altitudes during June (left) and December (right) solstices under the high solar activity condition. The blue, magenta, red and green lines stand for the four longitudinal sectors, as indicated by the same colored rectangles in the bottom of Figure 1. The solid and

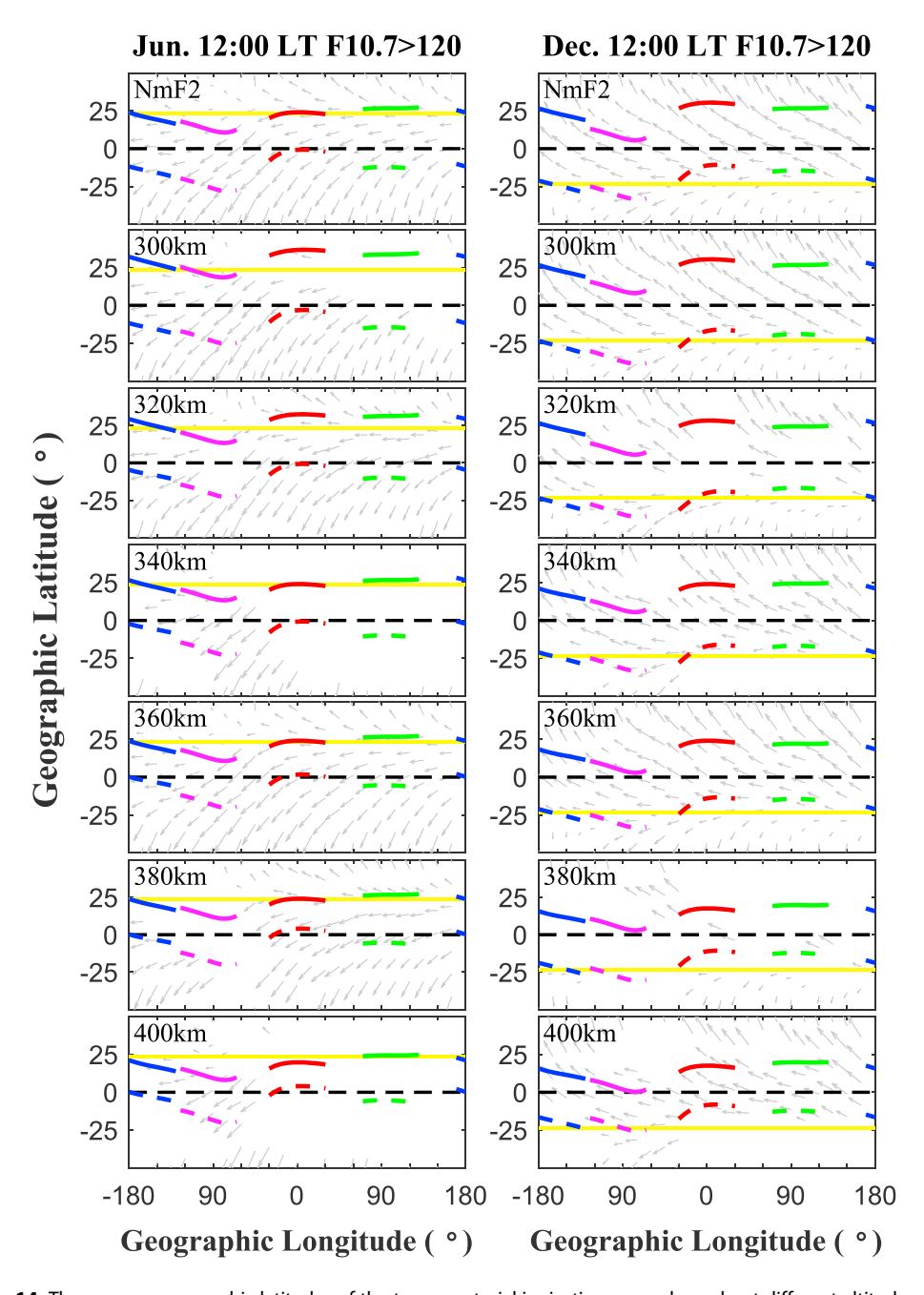


Figure 14. The average geographic latitudes of the two equatorial ionization anomaly peaks at different altitudes during June (left) and December (right) solstices under the high solar activity condition. The blue, magenta, red, and green lines stand for the four longitudinal sectors indicated by the same colored rectangles in the bottom of Figure 1. The solid and dash lines illustrate the north and south equatorial ionization anomaly peak locations. The yellow line indicates the latitude of the subsolar point. The gray arrows superposed in the figure are the neutral winds calculated by the Thermosphere lonosphere Mesosphere Electrodynamics General Circulation Model with the same scale for the winds in each panel.

dashed lines illustrate the northern and southern peak locations. The yellow line indicates the latitudes of subsolar points in the two hemispheres for June and December solstice conditions. The gray arrows superposed in the figure are the neutral winds calculated by the TIME-GCM with the same scale in each panel. The TIME-GCM is a three-dimensional time-dependent model that simulates the circulation, temperature, and compositional structure of the middle and upper atmosphere and the electron density in the ionosphere (Roble et al., 1998; Roble & Ridley, 1994; Liu & Roble, 2002). It extends from ~30 to above 500 km with a vertical resolution of ¼ scale height. The model was run with the horizontal



resolution of $2.5^{\circ} \times 2.5^{\circ}$ (latitude \times longitude) for the two solstices and for high and low solar activity levels, respectively. It can be seen from the left column of Figure 14 for the June case that the latitudes of EIA peaks in the magenta sector are further away from the latitude of the subsolar point in the summer (northern) hemisphere, experiencing a larger wind, as compared to those in other longitudes. Whereas in the red sector, EIA peaks are closer to the latitude of subsolar point, encountering a smaller wind. A large wind transports more plasma to higher (lower) altitude in the summer (winter) hemisphere. Hence, the transition time is earlier in the sector where neutral wind is large, which corresponds to the magenta sector and consistent with the results during the June solstice shown in the top two panels of Figure 8. Similarly, during the December solstice (right column of Figure 14), EIA peaks in the red sector are further away from the latitude of subsolar point, compared with the magenta sector. Hence, the red sector experiences larger neutral winds causing an earlier transition of the stronger peak to the summer hemisphere than in the magenta sector during the December solstice.

4.3. Altitudinal Variation of the Transition Time

The effective scale height of plasma density is a mathematical parameter to quantify the altitudinal distribution of plasma density, which has a positive correlation with plasma temperature. As height increases, plasma temperature increases so that plasma density decreases slowly. According to Liu et al. (2008), the effective scale height of plasma density is larger in the summer hemisphere than in the winter hemisphere at low latitudes during the daytime due to the higher plasma temperatures in the summer. Therefore, the electron density decreases slower in the summer hemisphere with altitude, compared to the winter hemisphere case. The electron density difference between the winter and summer hemispheres becomes smaller as height increases, which is shown in Figures 9 and 10. The smaller differences at high altitudes require less amount of time to transit, which explains the fact that the transition time occurs earlier at higher altitudes. We also examine the diurnal variation of the interhemispheric asymmetry of EIA at 480 km following Xiong et al. (2013) who reported that the summer hemisphere EIA was always larger than the winter one. However, our work shows that under most conditions the two peaks of the EIA have already merged into one single peak at higher altitudes under both low and high solar activity conditions. This discrepancy is probably related to the fact that the period of solar cycle 23 of their work.

5. Conclusions

In this work, the transition of the stronger EIA peak from the winter hemisphere to the summer hemisphere during the daytime has been studied by using COSMIC IRO EDP data. The diurnal variation of O/N_2 ratio in the two hemispheres along with the more intense solar radiation in the summer hemisphere and vertical plasma transport caused by the neutral winds are likely the possible mechanisms for the transition. The longitudinal and altitudinal variations of the transition time are examined systematically in four longitudinal sectors and at hmF2, and for altitudes every 20 km from 300 to 400 km for the first time. The major results are summarized as follows:

- 1. The longitudinal sector where \mathbf{U}_i and \mathbf{V}_i are in the same direction has an earlier transition time, whereas the transition time occurs later where \mathbf{U}_i and \mathbf{V}_i are in the opposite directions. Another factor that influences the longitudinal variation of the transition time is the relative distance between the latitude of subsolar point and geomagnetic equator in different longitudinal sectors. Longer/shorter distance results in larger/smaller cross-equator neutral winds. These two factors can either enhance or reduce plasma transport in the vertical direction, depending on the geomagnetic field configuration in different longitudes, and lead to different transition times.
- 2. The earlier transition at higher altitude is mainly caused by the larger effective scale height in the summer hemisphere and the resultant smaller differences in the electron density between the two hemispheres.
- 3. Solar activity alters the transition time below 320 km but has no obvious effects on the longitudinal and altitudinal variations of the transition time at higher altitudes.

An interesting feature is that the transition is delayed by about 2 hr during the June solstice compared with that in the December solstice. The ionospheric annual asymmetry seems to be a possible reason. Previous researchers utilized different models to investigate the impacts of photochemical process, ambipolar diffusion, and the Sun-Earth distance difference between June and December solstices on the electron density



distributions (Dang et al., 2017; Rishbeth & Müller-Wodarg, 2006; Zeng et al., 2008). They found that the Sun-Earth distance difference between June and December could strongly impact the electron density distributions, which may further affect the transition time and lead to its difference. The relationship between the 2-hr delay and annual asymmetry and the cause of it require further investigations. Another future work topic is to explain the fact that the longitudinal variation of the transition time is stronger during the June solstice, as compared with that in the December solstice case. We will focus on these topics using more data as well as model simulations in our future work.

Acknowledgments

We would like to express our thankfulness to the following affiliations for providing the data used in this study. COSMIC constellation IRO data are obtained from the COSMIC Data Analysis and Archive Center (http:// cdaac-www.cosmic.ucar.edu/cdaac/ products.html). F10.7 and Ap are downloaded from the National Geophysical Data Center (ftp://ftp.ngdc. noaa.gov). The GUVI data (O/N₂ ratio) used here are provided through support from the NASA Mission Operations and Data Analysis program. The GUVI instrument was designed and built by The Aerospace Corporation and The Johns Hopkins University, The Principal Investigator is Andrew B. Christensen and the Chief Scientist and co-PI is Larry J. Paxton. The National center for Atmospheric Research is sponsored by the National Science Foundation. This research is supported by the National Natural Science Foundation of China (41704157, 41774161, amd 41621063) and China Postdoctoral Science Foundation (2016 M601120), Xian Lu's work is supported by NASA HSR NNX17AG10G, and NSF grants AGS-1343106/1705448 (CEDAR), OPP-1543373/1705450, and AGS-1753214 (CAREER) award.

References

- Abur-Robb, M. F. K., & Windle, D. W. (1969). On the day and night reversal in NmF2 north-south asymmetry. *Planetary and Space Science*, 17(1), 97–106. https://doi.org/10.1016/0032-0633(69)90126-3
- Appleton, E. V. (1946). Two anomalies in the ionosphere. *Nature (London)*, 157(3995), 691. https://doi.org/10.1038/157691a0
- Balan, N., Bailey, G. J., Abdu, M. A., Oyama, K. I., Richards, P. G., MacDougall, J., & Batista, I. S. (1997). Equatorial plasma fountain and its effects over three locations: Evidence for an additional layer, the f3 layer. *Journal of Geophysical Research*, 102(A2), 2047–2056. https://doi.org/10.1029/95ja02639
- Balan, N., Rajesh, P. K., Sripathi, S., Tulasiram, S., Liu, J. Y., & Bailey, G. J. (2013). Modeling and observations of the north-south ionospheric asymmetry at low latitudes at long deep solar minimum. *Advances in Space Research*, 52(3), 375–382. https://doi.org/10.1016/j.asr.2013.04.003
- Bilitza, D. (2009). Evaluation of the iri-2007 model options for the topside electron density. *Advances in Space Research*, 44(6), 701–706. https://doi.org/10.1016/j.asr.2009.04.036
- Chen, Y., Liu, L., Le, H., Wan, W., & Zhang, H. (2016). Equatorial ionization anomaly in the low-latitude topside ionosphere: Local time evolution and longitudinal difference. *Journal of Geophysical Research: Space Physics*, 121, 7166–7182. https://doi.org/10.1002/2016JA022394
- Chu, Y.-H., Su, C.-L., & Ko, H.-T. (2010). A global survey of cosmic ionospheric peak electron density and its height: A comparison with ground-based ionosonde measurements. Advances in Space Research, 46(4), 431–439. https://doi.org/10.1016/j.asr.2009.10.014
- Croom, S., Robbins, A., & Thomas, J. O. (1959). Two anomalies in the behaviour of the f2 layer of the ionosphere. *Nature*, 184(4704), 2003–2004. https://doi.org/10.1038/1842003a0
- Dang, T., Luan, X., Lei, J., Dou, X., & Wan, W. (2016). A numerical study of the interhemispheric asymmetry of the equatorial ionization anomaly in solstice at solar minimum. *Journal of Geophysical Research: Space Physics, 121,* 9099–9110. https://doi.org/10.1002/201618023012
- Dang, T., Wang, W., Burns, A., Dou, X., Wan, W., & Lei, J. (2017). Simulations of the ionospheric annual asymmetry: Sun-earth distance effect. Journal of Geophysical Research: Space Physics, 122, 6727–6736. https://doi.org/10.1002/2017JA024188
- Duncan, R. A. (1960). The equatorial F-region of the ionosphere. *Journal of Atmospheric and Terrestrial Physics*, 18(2-3), 89–100. https://doi.org/10.1016/0021-9169(60)90081-7
- Guo, P., Xu, X., & Zhang, G. (2011). Analysis of the ionospheric equivalent slab thickness based on ground-based GPS/TEC and GPS/COSMIC RO measurements. *Journal of Atmospheric and Solar-Terrestrial Physics*, 73(7-8), 839–846. https://doi.org/10.1016/j.jastp.2011.02.002
- Hanson, W. B., & Moffett, R. J. (1966). Lonization transport effects in the equatorial f region. *Journal of Geophysical Research*, 71(23), 5559–5572 . https://doi.org/10.1029/JZ071i023p05559
- He, M., Liu, L., Wan, W., Ning, B., Zhao, B., Wen, J., Yue, X.'a., et al. (2009). A study of the weddell sea anomaly observed by formosat-3/cosmic. Journal of Geophysical Research, 114, A12309. https://doi.org/10.1029/2009JA014175
- He, M., Liu, L., Wan, W., & Zhao, B. (2011). A study on the nighttime midlatitude ionospheric trough. *Journal of Geophysical Research*, 116, A05315. https://doi.org/10.1029/2010JA016252
- Hu, L., Ning, B., Liu, L., Zhao, B., Li, G., Wu, B., Huang, Z., et al. (2014). Validation of cosmic ionospheric peak parameters by the measurements of an ionosonde chain in China. *Annales Geophysicae*, 32(10), 1311–1319. https://doi.org/10.5194/angeo-32-1311-2014
- Huang, H., Liu, L., Chen, Y., Le, H., & Wan, W. (2016). A global picture of ionospheric slab thickness derived from gim tec and cosmic radio occultation observations. *Journal of Geophysical Research: Space Physics, 121*, 867–880. https://doi.org/10.1002/2015JA021964
- Huang, H., Chen, Y., Liu, L., Le, H., & Wan, W. (2015). An empirical model of the topside plasma density around 600 km based on ROCSAT-1 and Hinotori observations. *Journal of Geophysical Research: Space Physics, 120*, 4052–4063. https://doi.org/10.1002/2014JA020940
- Lei, J., Syndergaard, S., Burns, A. G., Solomon, S. C., Wang, W., Zeng, Z., Roble, R. G., et al. (2007). Comparison of cosmic ionospheric measurements with ground-based observations and model predictions: Preliminary results. *Journal of Geophysical Research*, 112, A07308. https://doi.org/10.1029/2006JA012240
- Lin, C. H., Hsiao, C. C., Liu, J. Y., & Liu, C. H. (2007). Longitudinal structure of the equatorial ionosphere: Time evolution of the four-peaked eia structure. *Journal of Geophysical Research*, 112, A12305. https://doi.org/10.1029/2007JA012455
- Lin, C. H., Liu, J. Y., Fang, T. W., Chang, P. Y., Tsai, H. F., Chen, C. H., & Hsiao, C. C. (2007). Motions of the equatorial ionization anomaly crests imaged by formosat-3/cosmic. *Geophysical Research Letters*, 34, L19101. https://doi.org/10.1029/2007gl030741
- Lin, C. H., Wang, W., Hagan, M. E., Hsiao, C. C., Immel, T. J., Hsu, M. L., Liu, J. Y., et al. (2007). Plausible effect of atmospheric tides on the equatorial ionosphere observed by the formosat-3/cosmic: Three-dimensional electron density structures. *Geophysical Research Letters*, 34, L11112. https://doi.org/10.1029/2007GL029265
- Liu, H.-L., & Roble, R. G. (2002). A study of a self-generated stratospheric sudden warming and its mesospheric-lower thermospheric impacts using the coupled TIME-GCM/CCM3. *Journal of Geophysical Research*, 107(D23), 4695. https://doi.org/10.1029/2001JD001533
- Liu, L., He, M., Wan, W., & Zhang, M.-L. (2008). Topside ionospheric scale heights retrieved from constellation observing system for meteorology, ionosphere, and climate radio occultation measurements. *Journal of Geophysical Research*, 113, A10304. https://doi.org/ 10.1029/2008JA013490
- Liu, L., Zhao, B., Wan, W., Ning, B., Zhang, M.-L., & He, M. (2009). Seasonal variations of the ionospheric electron densities retrieved from constellation observing system for meteorology, ionosphere, and climate mission radio occultation measurements. *Journal of Geophysical Research*, 114, A02302. https://doi.org/10.1029/2008JA013819
- Luan, X., Wang, P., Dou, X., & Liu, Y. C. M. (2015). Interhemispheric asymmetry of the equatorial ionization anomaly in solstices observed by cosmic during 2007–2012. *Journal of Geophysical Research: Space Physics*, 120, 3059–3073. https://doi.org/10.1002/2014JA020820



- Lyon, A. J., & Thomas, L. (1963). The f2-region equatorial anomaly in the African, American and East Asian sectors during sunspot maximum. Journal of Atmospheric and Terrestrial Physics, 25(7), 373–386. https://doi.org/10.1016/0021-9169(63)90170-3
- Rajaram, G. (1977). Structure of the equatorial F-region, topside and bottomside—A review. *Journal of Atmospheric and Terrestrial Physics*, 39(9-10), 1125–1144. https://doi.org/10.1016/0021-9169(77)90021-6
- Rao, C. S. R., & Malthotra, P. L. (1964). A study of geomagnetic anomaly during IGY. *Journal of Atmospheric and Terrestrial Physics*, 26(11), 1075–1085. https://doi.org/10.1016/0021-9169(64)90093-5
- Ren, Z., Wan, W., Liu, L., Zhao, B., Wei, Y., Yue, X., & Heelis, R. A. (2008). Longitudinal variations of electron temperature and total ion density in the sunset equatorial topside ionosphere. *Geophysical Research Letters*, *35*, L05108. https://doi.org/10.1029/2007GL032998
- Rishbeth, H., & Müller-Wodarg, I. C. F. (2006). Why is there more ionosphere in January than in July? The annual asymmetry in the f2-layer. Annales de Geophysique, 24(12), 3293–3311. https://doi.org/10.5194/angeo-24-3293-2006
- Roble, R. G., & Ridley, E. C. (1994). A thermosphere-ionosphere-mesosphere-electrodynamics general circulation model (time-GCM): Equinox solar cycle minimum simulations (30–500 km). Geophysical Research Letters, 21(6), 417–420. https://doi.org/10.1029/93GL03391
- Roble, R. G., Ridley, E. C., Richmond, A. D., & Dickinson, R. E. (1998). A coupled thermosphere/ionosphere general circulation model. Geophysical Research Letters, 15(12), 1325–1328. https://doi.org/10.1029/GL015i012p01325
- Stening, R. J. (1992). Modelling the low latitude f region. Journal of Atmospheric and Terrestrial Physics, 54(11-12), 1387–1412. https://doi.org/10.1016/0021-9169(92)90147-D
- Thomas, L. (1968). The f2-region equatorial anomaly during solstice periods at sunspot maximum. *Journal of Atmospheric and Terrestrial Physics*, 30(9), 1631–1640. https://doi.org/10.1016/0021-9169(68)90011-1
- Tulasi Ram, S., Su, S. Y., & Liu, C. H. (2009). FORMOSAT-3/COSMIC observations of seasonal and longitudinal variations of equatorial ionization anomaly and its interhemispheric asymmetry during the solar minimum period. *Journal of Geophysical Research*, 114, A06311. https://doi.org/10.1029/2008JA013880
- Walker, G. O., Ma, J. H. K., & Golton, E. (1994). The equatorial ionospheric anomaly in electron content from solar minimum to solar maximum for South East Asia. *Annales de Geophysique*, 12(2/3), 195–209. https://doi.org/10.1007/s00585-994-0195-0
- Xiong, C., Lühr, H., & Ma, S. Y. (2013). The magnitude and inter-hemispheric asymmetry of equatorial ionization anomaly-based on CHAMP and GRACE observations. *Journal of Atmospheric and Solar-Terrestrial Physics*, 105-106, 160–169. https://doi.org/10.1016/j. jastp.2013.09.010
- Yue, X., Schreiner, W. S., Kuo, Y.-H., & Lei, J. (2015). Ionosphere equatorial ionization anomaly observed by GPS radio occultations during 2006–2014. *Journal of Atmospheric and Solar-Terrestrial Physics*, 129, 30–40. https://doi.org/10.1016/j.jastp.2015.04.004
- Yue, X., Schreiner, W. S., Lei, J., Sokolovskiy, S. V., Rocken, C., Hunt, D. C., & Kuo, Y. H. (2010). Error analysis of abel retrieved electron density profiles from radio occultation measurements. *Annales de Geophysique*, 28(1), 217–222. https://doi.org/10.5194/angeo-28-217-2010
- Zeng, Z., Burns, A., Wang, W., Lei, J., Solomon, S., Qian, L., et al. (2008). Ionospheric annual asymmetry observed by the cosmic radio occultation measurements and simulated by the TIEGCM. *Journal of Geophysical Research*, 113, A07305. https://doi.org/10.1029/2007JA012897 Zhang, R., Liu, L., Le, H., & Chen, Y. (2016). Evidence and effects of the sunrise enhancement of the equatorial vertical plasma drift in the f
- region ionosphere. Journal of Geophysical Research: Space Physics, 121, 4826–4834. https://doi.org/10.1002/2016JA022491